ACS APPLIED ELECTRONIC MATERIALS

pubs.acs.org/acsaelm Article

Experimental and Theoretical Insights into the Structural Disorder and Gas Sensing Properties of ZnO

Bruno Sanches de Lima,* Paulina R. Martínez-Alanis, Frank Güell, Weverton Alison dos Santos Silva, Maria I.B. Bernardi, Naiara L. Marana, Elson Longo, Júlio R. Sambrano, and Valmor R. Mastelaro

Cite This: https://dx.doi.org/10.1021/acsaelm.1c00058 Read Online

ACCESS | Metrics & More | Article Recommendations | Supporting Information

ABSTRACT: Recently, it was demonstrated that ZnO thin films sputtered under oxygen-rich atmospheres exhibit localized structural disorder with a significant impact on their physical properties due to the presence of high energetic ions in the plasma. Here, highly disordered ZnO thin films have been realized simply by using a metallic Zn target under a deposition atmosphere of pure oxygen (O_2). The results of XRD and Raman spectroscopy show that the defects induced during the deposition crystallize a highly disordered wurtzite-type structure. In addition, theoretical DFT calculations were applied for a better comprehension of the nature of these structural defects, in which it is shown that the presence of Zn and O in interstitial positions may be responsible for a symmetry break in the wurtzite structure. It is shown that high disorder of the structure has a significant impact on its fundamental properties. For instance, the UV−vis absorption curve shows a significant increase in the bandgap of ZnO, while photoluminescence (PL) measurements show the emergence of bands in the visible range, confirming the presence of Zn and O in interstitial positions. This manuscript also explores the gas sensing properties of films deposited under a pure oxygen atmosphere. Our results demonstrate that their sensitivity can be significantly enhanced toward oxidizing gas detection, such as ozone. On the other hand, it is shown that the gas sensing properties regarding reducing gas detection, such as H_2, are not significantly altered when compared to non-disordered ZnO.

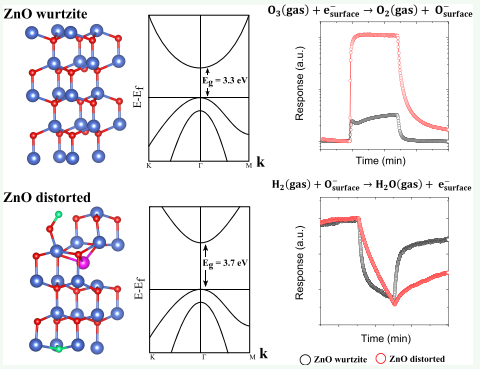

KEYWORDS: *ZnO, structural disorder, RF magnetron sputtering, reactive atmosphere, gas sensor*

1. INTRODUCTION

Zinc oxide (ZnO) is an important material in the semiconductor industry due to its remarkable properties related to its wide and direct bandgap of ∼3.3 eV.[1] Interestingly, its n-type semiconducting nature has been historically pointed out due to naturally occurring oxygen vacancies in the crystal structure.[2−4] Still, more recent theoretical development suggests that O vacancies are deep donors and its n-type conductivity is attributed to group III impurities.[5] Among the different phases in which ZnO can be found, the wurtzite structure is the most stable. It grants ZnO great versatility as it is possible to grow this oxide in different nanostructured morphologies.[6] As a consequence, this semiconductor material has been successfully applied in solar cells,[7] chemical sensors,[8] or as a high-efficiency photocatalytic material.[9]

Radio-frequency (RF) magnetron sputtering is an important technique used to produce high-quality ZnO-based thin films and devices. This technique is versatile because by tuning the deposition parameters, one can control the films' morphology, grain size, thickness, and physical properties.[10,11] For instance, it was demonstrated that the oxygen ratio during deposition could change ZnO optical properties.[12] Several authors also reported the formation of highly oriented (002) ZnO thin films when metallic Zn targets are used under an O_2-rich atmosphere or when ceramic ZnO targets are used.[13−16] It was also shown that ZnO deposition using a metallic Zn target and O_2-rich atmosphere could be used as a parameter to tune ZnO gas sensing properties.[15−17] Suchea et al.[17] demonstrated that ZnO films deposited using metallic and ceramic targets could significantly alter ZnO's outcome properties. Furthermore, their results showed that by employing a metallic Zn target and O_2 reactive atmosphere, these films' sensitivity could be enhanced regarding ozone detection.

Some studies pointed out that oxygen-rich atmospheres during RF magnetron sputtering processes play a crucial role in the dynamics of defect formation of the ZnO lattice and might be the primary mechanism responsible for changes in its physical properties. In 1985, the work of Tominaga et al.[18] showed that an oxygen-rich plasma is composed mainly of

Received: January 18, 2021
Accepted: March 2, 2021

https://dx.doi.org/10.1021/acsaelm.1c00058
ACS Appl. Electron. Mater. XXXX, XXX, XXX−XXX

highly energetic O atoms and O^- ions with a significant impact on the electrical properties of ZnO films. Other ions, such as ZnO^- and ZnO_2^-, were also observed during Al-doped ZnO sputtering deposition.[19,20]

ZnO exhibits four types of intrinsic point defects: vacancies and interstitials of Zn and O, namely, V_{zn}, Zn_i, V_O, and O_i, respectively.[2] First principle calculations show that oxygen vacancies (V_O) have the lowest formation energy among the four mentioned defects when ZnO is prepared under both Zn- or O-rich conditions.[21] Consequently, these defects are dominant. Under O-rich conditions, however, the formation energy of O_i is comparable to the formation of V_O.[21] Recently, Meng et al.[22] showed that local disorder could be induced in Al-doped ZnO by superimposing DC discharges onto RF discharges in an Al-doped ceramic ZnO target as a way of controlling O^- bombardment on the target surface.

Within this context, we present experimental data on thin films grown by RF magnetron sputtering using a metallic zinc target deposited under a pure O_2 atmosphere. The results of X-ray diffraction and Raman spectroscopy demonstrate that the deposition under these conditions crystallizes a highly disordered wurtzite-type structure. Theoretical DFT calculations of the Raman spectra confirmed the presence of Zn and O atoms in the octahedral interstitial sites. X-ray photoelectron spectroscopy shows that ZnO thin films deposited under O_2 have a richer peroxide (O^-) component than conventional ZnO, and the UV−vis absorbance spectra show a bandgap energy of 3.7 eV, which is significantly higher than the bandgap of 3.3 eV observed for ZnO. Photoluminescence measurements show a very broad emission band in the visible range from 420 to 850 nm, which exhibits distinct peak-like contributions at approximately 490, 510, 620, and 770 nm related to different defect recombination processes. The peaks at near-infrared nm correspond to emissions due to the presence of O_i. Furthermore, we present a comparative study of the gas sensing properties of ZnO thin films prepared under O_2 and Ar regarding ozone and hydrogen detection. Our results show that defects in the ZnO structure can be used to tune its sensing properties as the disordered thin films exhibit a higher response for ozone detection than conventional ZnO, while their sensing properties are not significantly altered toward H_2 detection.

2. EXPERIMENTAL PROCEDURE

2.1. Thin Film Deposition. Thin films were sputtered using a high-purity metallic zinc target (99.95%) with 3 in. of diameter, at 6.5 cm from the substrates, and RF power set to 50 W. Initially, the deposition chamber was kept under high vacuum (5×10^{-6} mbar) for 1 h. The pressure during deposition was fixed at 2.5×10^{-2} mbar with either pure oxygen (O_2) or pure argon (Ar). These films were deposited on silicon or glass substrates freshly cleaned according to the RCA standard procedure. The thickness of the films was estimated using a Taylor Hobson Talystep profilometer. After deposition, these films were heat treated under air for 12 h. Table 1 summarizes the sample preparation conditions.

2.2. Thin Film Characterization. X-ray diffraction data were collected in a Rigaku Ultima IV diffractometer within the range of $2\theta = 20-60°$ using Cu Kα radiation (λ = 1.5418 Å) and a LiF (100) monochromator in the conventional $\theta-2\theta$ configuration. The diffraction experiments were carried out in films deposited in glass substrates with a thickness of approximately 1 μm. The data analysis was performed with GSAS-II[23] and VESTA crystallography.[24]

Micro-Raman spectra were collected in a Witec (Ulm, Germany) microscope equipped with a highly linear stage and objective lens from Nikon (100 × NA = 0.9). Our samples were excited with an ion argon laser (514 nm; 10 mW), and the Raman signal was measured with a back-illuminated Peltier-cooled CCD located behind a 1800 grooves/mm grating.

Table 1. Summary of Sample Preparation Conditions

label	deposition atmosphere	heat-treatment temperature (°C)
ZnO-Ar-550	argon	550
ZnO-O_2-RT	oxygen	
ZnO-O_2-550	oxygen	550
ZnO-O_2-750	oxygen	750
ZnO-O_2-1000	oxygen	1000

X-ray photoelectron spectroscopy (XPS) measurements were carried out in a Scientia Omicron ESCA spectrometer with a monochromatic X-ray source Al Kα (1486.7 eV, with a power of 280 W and a constant pass energy mode of 50 eV). The XPS spectral analysis was carried out using CasaXPS software. The obtained values of binding energy were corrected, assuming 284.8 eV for adventitious carbon.

UV−Vis spectroscopy measurements were carried out on films deposited on quartz substrates in a Shimadzu-1800 spectrometer. Film morphology and cross section were examined by scanning electron microscopy (SEM) (Zeiss DSM 960 model).

Room-temperature photoluminescence (PL) spectra were recorded with a chopped Kimmon IK Series He-Cd laser (325 nm and 40 mW). Fluorescence was dispersed through a SpectraPro 2750 (focal length: 750 mm) f/9.8 monochromator, detected with a Hamamatsu H8259-02 photomultiplier, and amplified through a Stanford Research Systems SR830 DSP lock-in amplifier. A 360 nm filter was used to filter the stray light. All spectra were corrected for the response function of the setups.

2.3. Computational Methods. DFT simulations were conducted using the CRYSTAL17 program[25] in association with the default B3LYP[26] hybrid functional and all-electron basis set, which describes the atomic centers of zinc (86-411d31G)[27] and oxygen (8-411d1)[28] atoms. The vibrational frequencies at the Γ point were computed within the harmonic approximation by diagonalizing the mass-weighted Hessian matrix as implemented in the CRYSTAL code.[29,30] This methodology was applied in the previous ZnO study and demonstrated great accuracy with the experimental results.[31,32]

In the first step, the ZnO wurtzite bulk was obtained, and its atomic coordinates and cell parameters were optimized to minimize the total energy. The cell (a and c) and internal (u) optimized parameters are 3.274 Å, 5.250 Å, and 0.383, respectively, and are in good agreement with available experimental data.[33,34] In order to obtain a more realistic model to evaluate the effect of Zn and O in the interstitial site, a 2 × 2 × 2 supercell with 32 atoms (16 oxygen and 16 zinc) was constructed from the optimized ZnO bulk.

To analyze the influence of each atom in the interstice and to predict the structural defects observed experimentally, by comparing the theoretical Raman spectra with experimental ones, the Zn and O atoms were separately inserted in the octahedral interstice of the ZnO supercell and reoptimized. The third model considered both Zn and O in octahedral interstices, and the structure was reoptimized (see Figure S1). Subsequently, the three models have their frequencies calculated as well as their Raman spectra. It is important to emphasize that all analyzed models with the atoms in the interstice did not have any negative frequencies, which indicates that the theoretical structures are stable and that all possibilities can experimentally occur.

2.4. Sensor Fabrication and Gas Sensing Performance. The gas sensor devices were fabricated upon deposition of 100 nm-thick Pt-interdigitated electrodes over Si−SiO_2 substrates. The sensing layer was deposited over the Pt electrodes, and the thickness was controlled by the deposition time. The gas sensing devices were then heat treated at 550 °C for 12 h. These devices were placed over a heating element inside a homemade chamber with a gas inlet, outlet, and cables connecting the Pt electrodes to a Tektronix PWS4205 voltage source. The electrical current flowing through these two Pt terminals was monitored with a Keithley 6514 electrometer. One can calculate

https://dx.doi.org/10.1021/acsaelm.1c00058
ACS Appl. Electron. Mater. XXXX, XXX, XXX−XXX

the electrical resistance of the sensing material by the ratio of the applied voltage and measured current. The measurements presented in this report were carried out using a total flux of 100 cm^3/min of dry air flowing directly to the film surface. The sensor response (S) is defined as $R_{analyte}/R_{air}$. In order to study the material response under O_3, the devices were exposed to ozone generated by exposing the dry airflow to a pen-ray UV lamp (UVP, model P/N 90-0004-01). Its response to reducing gases was evaluated upon exposure to a gas mixture of dry air and H_2. The concentrations of O_3 and H_2 were determined by an ATI (model F12) commercial gas detector. The response time is defined as the time necessary to reach 90% of the resistance saturation for a specific gas concentration. O_3 and H_2 were chosen because these gases are suitable to explore the gas sensing properties of SMOx-based sensors since the dynamics of charge transfer of both species are based on the surface oxygen species chemisorbed in the SMOx surface and have been used as models for fundamental research on the mechanisms of SMOx gas sensing properties.[35,36]

3. RESULTS AND DISCUSSION

3.1. Structural Characterization. Figure 1a presents typical X-ray diffraction patterns obtained from ∼1 μm-thick

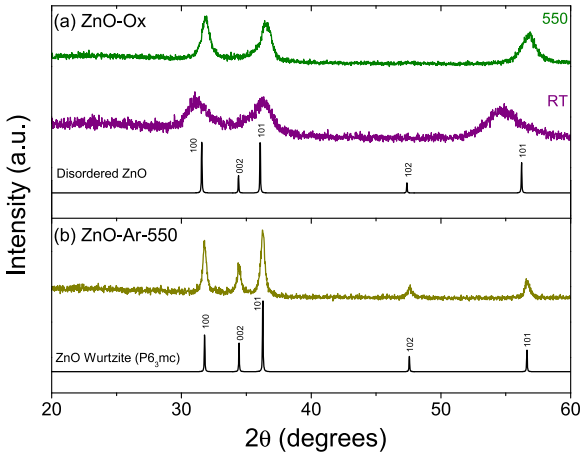

Figure 1. X-ray diffraction pattern of films obtained when deposited under (a) pure oxygen and (b) pure argon followed by a 12 h heat treatment.

films deposited under pure O_2 without heat treatment (ZnO-O_2-RT) and after heat treatment at 550 °C for 12 h under air (ZnO-O_2-550). These films were deposited over silicon substrates, and it is possible to observe broad diffraction peaks that have intensities comparable to the background. By assuming that the crystalline regions of these films have symmetry similar to the wurtzite-type structure (SG $P6_3mc$), the observed diffraction peaks at 2θ = 31.5, 36.5, and 56.5° should be related to planes (100), (101), and (110), respectively. It is interesting to note that these films do not exhibit reflections related to (002) and (102), which suggest the presence of texture on these samples.

Figure 1b shows the diffraction pattern of an ∼1 μm-thick film prepared by metallic Zn deposition under an Ar atmosphere followed by heat treatment at 550 °C for 12 h under air (ZnO-Ar-550). In this case, the typical ZnO wurtzite diffraction pattern is well defined, and samples prepared similarly will be used as controls in this study. Another feature that should be noted within this XRD data set is the relative intensities of the (100) and (101) reflections. In samples deposited under O_2, the highest intensity reflection is related to the (100) peak, while in the typical wurtzite-type structure, the highest intensity peak is (101).

Rietveld refinement was carried out using the XRD data from samples prepared under O_2 (ZnO-O_2-550) and Ar (ZnO-Ar-550) atmospheres as shown in Figure 1a,b. Under an Ar atmosphere, the refinement was stable and converged fast, yielding lattice parameters of a = 3.25 and c = 5.21 Å and a goodness of fit of 1.99 considering typical ZnO tetragonal $P6_3mc$ wurtzite, which is in agreement with the literature.[37] Under O_2, on the other hand, the refinement was stable when another oxygen atom was considered in the crystal structure of ZnO. In this case, the refinement yielded lattice parameters of a = 3.26 and c = 5.31 and a goodness of fit of 1.51. In addition to the difference observed in the relative intensities of the XRD patterns, the increase (0.1 Å) in the c lattice parameter could also be pictured as evidence of distortion of the wurtzite unit cell in samples prepared under O_2. Figure S2 presents the XRD pattern simulation of the final refined structure. It is important to note that these results only suggest atoms in interstice positions, which will be appropriately addressed in the DFT section. As shown in Figure S2, by considering two oxygen atoms in the wurtzite crystal structure, one can note that the intensity of the peak (100) becomes higher than the peak (101), as observed in the experimental data shown in Figure 1.

In Figure S3, the effect of heat treatment on the crystalline structure of ZnO-O_2 samples was also analyzed by XRD. It is possible to observe that as the temperature of the heat treatment rises, the (101) reflection becomes more intense than the (100), and the diffraction peaks become well defined, which suggests that the ZnO wurtzite structure could be partially restored. Peaks related to the formation of zinc silicate Zn_2SiO_4 (space group $R\bar{3}$) are observed in the samples treated at 750 and 1000 °C due to a reaction between the film and the substrate. Interestingly, the peak in the vicinity of 34° should be related to the (410) diffraction peak of the Zn_2SiO_4 cell as it shifts toward lower values as the temperature rises. The (002) diffraction peak of the wurtzite structure should be centered at 34.5°. These results suggest that some level of disorder in the wurtzite structure is persistent even at higher temperatures.

Raman spectroscopy measurements were carried out to better understand the effect of the O_2 atmosphere during deposition on the ZnO's wurtzite structure. Figure 2a shows the Raman spectra of a film deposited under O_2 and Figure 2b under Ar; both were heat treated at 550 °C for 12 h. The Raman spectra of the ZnO phase exhibit six first-order peaks related to the A_1, E_1, and E_2 optical phonon modes.[38] The two most intense peaks in the ZnO spectra are located close to 99 and at 438 cm^{-1}. These peaks are the result of two degenerate E_2 phonon modes of the Zn and O sublattice vibration, namely, E_2^{low} and E_2^{high}, respectively. The multiphonon combination of these two modes (E_2^{high}–E_2^{low}) generates a small peak in the vicinity of 330 cm^{-1} of the Raman spectra. The A_1 and E_1 optical phonons are also infrared active. Hence, they split into transversal and longitudinal components, which results in four peaks in the spectra, namely, A_1(TO) ≈ 380, A_1(LO) ≈ 574, E_1(TO) ≈ 407, and E_1(LO) ≈ 583 cm^{-1}.[38] The peaks observed in samples deposited under Ar (Figure 2b) at 382, 419, 439, 579, and 586 cm^{-1} were attributed to A_1(TO), E_1(TO), E_2^{high}, A_1(LO), and E_1(LO) vibration modes, respectively. The peaks observed at 535, 662, 1110, and 1157 cm^{-1} are related to second-order modes. By comparing the spectra of films deposited under O_2 (Figure 2a) and Ar (Figure 2b), one can easily note that the main

https://dx.doi.org/10.1021/acsaelm.1c00058
ACS Appl. Electron. Mater. XXXX, XXX, XXX−XXX

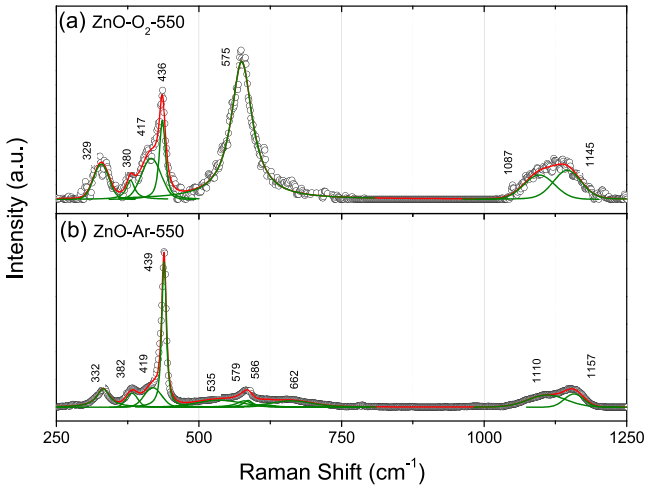

Figure 2. Raman spectra obtained from films deposited under (a) O_2 and (b) Ar followed by a 550 °C heat treatment for 12 h. The intensity enhancement of the bands in the vicinity of 579 cm^{-1} is related to the formation of crystalline defects.

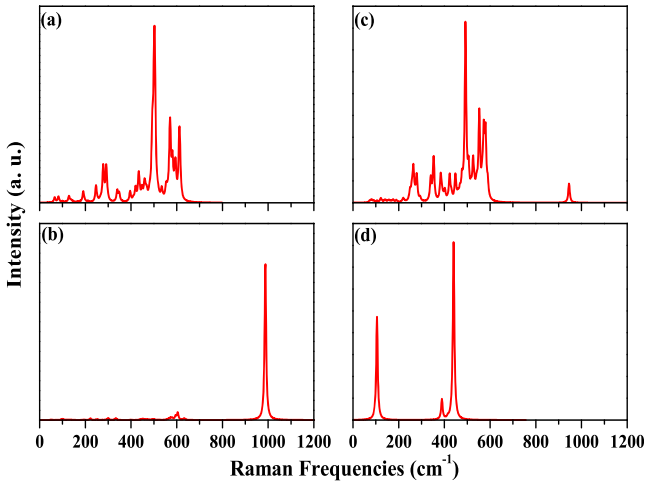

Figure 3. Calculated Raman spectra considering (a) Zn, (b) O, and (c) both Zn and O in the interstice octahedral position. (d) Calculated Raman spectra of bulk ZnO.

difference between these two samples lies in a significant enhancement of the bands A_1(LO) and E_1(TO). As these bands are related to the longitudinal vibration of oxygen and zinc atoms, they should be sensitive to the presence of point defects. For instance, Cerqueira and collaborators demonstrated that ZnO films deposited via molecular beam epitaxy do not exhibit the peaks related to the modes A_1(LO) and E_1(LO).[39] Similarly, the very intense peak observed at 575 cm^{-1} in Figure 2a is attributed to a convolution of the A_1(LO) and E_1(LO) bands. This peak is also observed in ZnO nanowires,[40] in which oxygen point defects are present due to the high surface-to-volume ratio of these nanostructures.

3.2. Theoretical Results. As the experimental results suggested the massive presence of interstitial defects, the O and Zn atoms in the ZnO interstice were theoretically analyzed following the methodology described in Section 2.3. Data from the literature suggest that Zn and O atoms in octahedral interstices are the most stable defects, and the diffusion of these atoms is more likely to occur instead of tetrahedral interstices.[41,42] Therefore, all the tests of the interstitial atoms were performed considering the octahedral interstice on the ZnO supercell. Figure S1 presents the ZnO bulk supercell, with and without Zn and O, in octahedral interstitial positions. As seen in Figure S1, all the analyzed systems have a small distortion in their structures after the optimization, which causes a break in symmetry. It was observed that the oxygen in the interstitial distorts the structure more than zinc in a similar interstitial position. However, when both kinds of defects are considered, the distortion in the structure is greater than the distortion observed when only one kind of defect is considered.

Figure 3 presents the calculated Raman spectra for the three models of ZnO with Zn, O, and both Zn and O atoms occupying octahedral interstice positions. After the interstitial atom additions, the material preserves its structure as confirmed by the presence of Raman vibrational modes of bulk ZnO, shown in Figure 3d, at ~100 and 450 cm^{-1}. The Raman spectra of the model with interstitial O, shown in Figure 3b, exhibit a characteristic peak at ~1000 cm^{-1} that corresponds to a peroxide mode (O−O bond of 1.46 Å in length). The same peak can be found in the experimental Raman spectrum (at ~1100 cm^{-1}), which suggests that the experimentally synthesized material presents interstitial oxygen with a peroxide bond. Another interesting feature observed in these experimental−theoretical analyses is the presence of interstitial zinc. Figure 3a demonstrates its vibrational modes between 100 and 450 cm^{-1} and after 500 cm^{-1}, which is also observed in the experimental Raman spectrum. These vibrational modes can be attributed to modifications of the structure caused by Zn interstitial atoms as the vibrational modes at ~600 cm^{-1} are due to the Zn_i-O bond stretching.

To complete the analysis, the model with Zn and O interstitial had its structure fully optimized (atomic coordinates, volume, and cell parameters) to confirm the structural stability. Figure 3c shows the Raman spectrum after full optimization. It can be observed that not only the vibrational modes of ZnO bulk are maintained but also the characteristic peaks at ~550 and ~950 cm^{-1} that correspond to the Zn and O interstitial, respectively. The optimized cell parameters are a = 3.295 and c = 5.580 Å. This corresponds to an increase of 0.02 and 0.33 Å in a and c lattice parameters of bulk ZnO, respectively. The XRD data also suggested a more significant increase in the c lattice parameter than in a. By comparing the Raman spectra of ZnO considering Zn and O atoms in octahedral interstice positions and bulk ZnO, shown in Figure 3c,d, one can note a small displacement in the peaks, which is due to the small rearrangements, caused by the symmetry break, of all atoms in the structure and the modifications along the c parameter.

3.3. Chemical Characterization. Figure 4 presents XPS measurements that were carried out to investigate the chemical surface state differences between films deposited under O_2 (yellow circles) and Ar (black circles). Figure 4a shows that the two films' XPS survey spectra deposited under different atmospheres are very similar. These spectra exhibit peaks related to Zn 2p1/2 (~1043 eV), Zn 2p3/2 (~1020 eV), O 1s (~532 eV), C 1s (~284.5 eV), Zn 3s (~141 eV), Zn 3p (~90 eV), and Zn 3d (~11 eV).[43] Figure 4b presents the high-resolution spectra of Zn 2p and shows that both spectra are very similar. In both samples, each of the two degenerated Zn 2p electron high-resolution spectra showed a symmetric peak that was fitted with only one component. Samples deposited

https://dx.doi.org/10.1021/acsaelm.1c00058
ACS Appl. Electron. Mater. XXXX, XXX, XXX−XXX

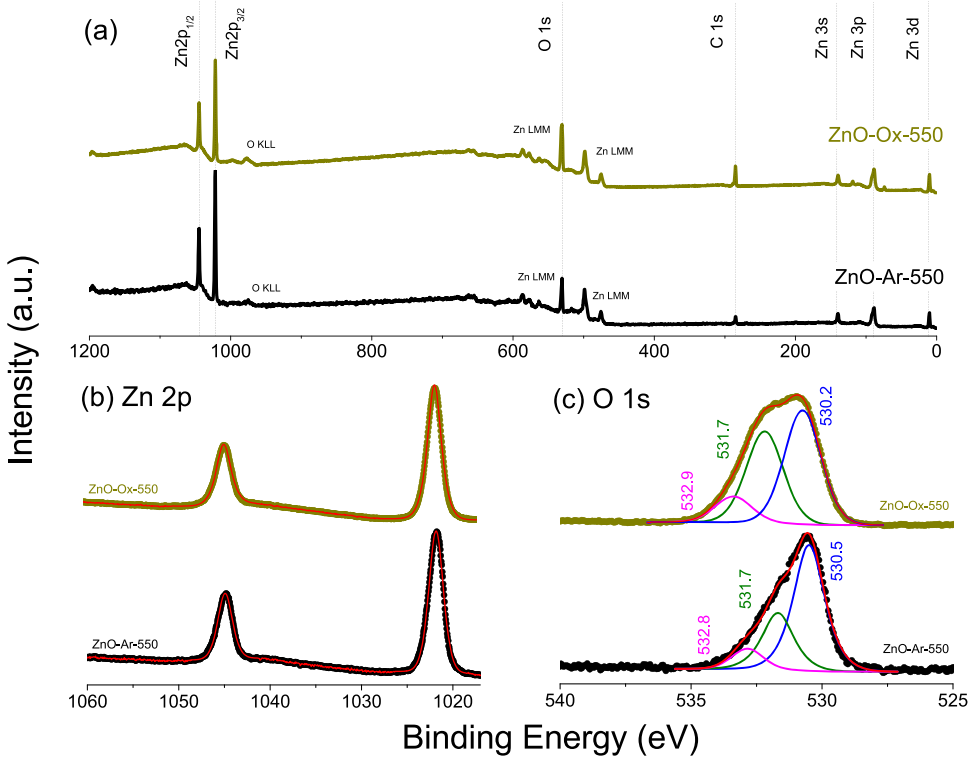

Figure 4. Comparison of XPS spectra obtained from Zn films deposited under Ar and O_2. Panel (a) shows the survey spectra, (b) Zn 2p high-resolution spectra, and (c) O 1s high-resolution spectra. It is possible to observe a larger O 1s peak related to the component at 531.7 eV related to the peroxide (O^-) form of oxygen.

under both Ar and O_2 show Zn 2p1/2 and Zn 2p3/2 binding energies of 1044.9 and 1021.8 eV, respectively.

The most significant difference between the XPS spectra of the films deposited under O_2 and Ar can be seen in the O 1s high-resolution spectra, shown in Figure 4c. Both conditions yielded films in which the O 1s electron peak can be deconvoluted into three components. Within the data of metallic zinc deposited under Ar followed by oxidation heat treatment (black circles), these three components are assigned to structural oxide ions (O^{2-}) at 530.5 eV, to weakly adsorbed species at the surface such as peroxide ions (O^-) or hydroxide ions (OH^-) at 531.8 eV, and to C−O bonds from adventitious carbon at 532.9 eV. These three components represent 61.5, 29.4, and 9.1% of the O 1s surface states, respectively. These results agree with the literature in which the component related to weakly adsorbed species (OH^- or O^-) represents approximately 25% of the O 1s surface states.[43,44] Now, by comparing both O 1s spectra, one can notice that the O 1s spectrum from the Zn films deposited under pure O_2 shows the same three components assigned to oxide ions (O^{2-}) at 530.2 eV, peroxide/ hydroxide (O^- or OH^-) at 531.7 eV, and C−O at 532.8 eV, with the only difference being the higher amount of the peroxide component region. In this case, the oxide, peroxide/hydroxide, and C−O components represent 47.5, 41.2, and 11.3% of the O 1s surface states, respectively. The significant increase in peroxide/hydroxide strongly suggests that samples prepared under O_2 exhibit another oxygen state in the wurtzite structure, which could be one reason for the structural distortion observed in the XRD data and A_1(LO) and E_1(LO) Raman peak intensity enhancement. Similar results can be found in the literature for oxygen-deficient samples. Hence, the O 1s component in the vicinity of 531.5 eV is frequently associated with defects in oxygen sites.[22,45,46] Figure S4 and Table S1 show the effect of the heat-treatment temperature on the relative amount of this O 1s component. These results show that this component is higher for samples treated at 550 °C. In other words, films prepared under O_2 and heat treated at temperatures in the order of 750 and 1000 °C exhibit a relative amount of this component similar to that observed for ZnO films oxidized under air. The evidence presented by the XPS results also suggests that the disorder observed in films deposited under O_2 is a consequence of the high density of defects in the wurtzite matrix structure.

3.4. Optical Characterization. Figure 5 presents the Tauc plot[47] considering $\gamma = 1/2$ for direct bandgap semiconductors obtained after the UV−vis absorbance spectra for films deposited under O_2 and Ar (inset). From the Tauc method, one can estimate the optical band gap of a semiconductor by considering the following equation: $(F(R_\infty)h\upsilon)^2 = c(h\upsilon - E_g)$. As seen in Figure 5, by plotting $(F(R_\infty)h\upsilon)^2$ versus $h\upsilon$, the optical band gap (E_g) is the $h\upsilon$-axis intercept of the tangent line on the inflection point of the Tauc plot curve, represented by the red dashed line. The bandgap energy is significantly higher for films deposited under O_2 (3.7 eV) than for films deposited under Ar (3.3 eV). A similar behavior has been observed for $SrTiO_3$, in which RF-magnetron sputtering induces an amorphous crystal structure with a higher bandgap than can be tuned upon thermal treatment.[48] For $SrTiO_3$, it is important to note that oxygen vacancies and substitutional effects play an important role in its fundamental physical properties.[49]

Figure 6 shows the room-temperature photoluminescence (PL) results. By pumping at 325 nm (3.8 eV), we have observed one peak in the UV range and a broad emission band

https://dx.doi.org/10.1021/acsaelm.1c00058
ACS Appl. Electron. Mater. XXXX, XXX, XXX−XXX

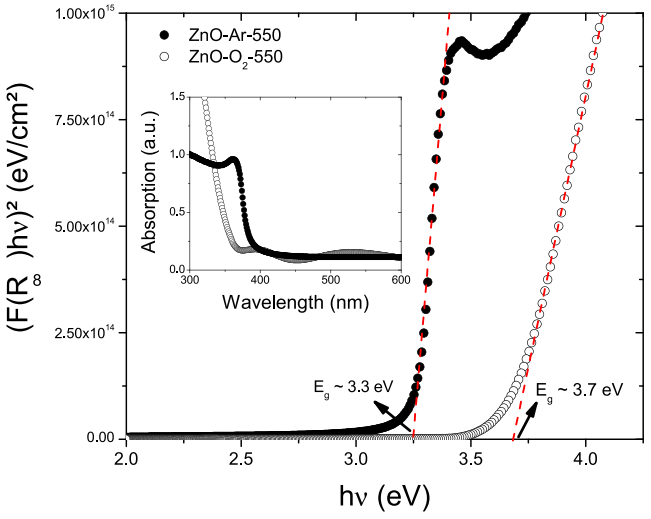

Figure 5. Tauc plot determined after the UV−vis absorbance spectra (inset) for films deposited under Ar and O_2, illustrating a significant enhancement of the band gap energy of ZnO films deposited under O_2.

in the visible range from 420 to 850 nm in all samples. Figure 6a presents the PL spectrum of a sample prepared by depositing metallic Zn under Ar with further heat treatment at 550 °C (ZnO-Ar-550). This spectrum agrees with previous PL results of ZnO published before.[50−55] The first UV peak can be deconvoluted into two components, one at 379 nm (3.27 eV) related to exciton formation or to the CB−VC transition and another component at 389 nm (3.19 eV) that have been attributed to a shallow donor level related to Zn_i.[53]

Now, let us turn the discussion to the broad emission observed in the visible range. According to the work of Janotti and Van de Walle,[50] the emissions in the visible range are related to the transition levels of V_O (2+/+), V_{Zn} (−/2−), and O_i (−/2−) are 2.51, 0.87, and 1.59 eV, respectively. Considering these values, the de-excitation of electrons trapped in shallow V_O would generate emissions with a wavelength of approximately 490 nm (2.51 eV), and the transitions from the conduction band to deep levels of V_{Zn} and O_i would have values of 2.36 and 1.64 eV, which corresponds to emissions with wavelengths of 520 and 760 nm, respectively. Indeed, the near-infrared emission at 760 nm of ZnO was successfully explained, considering that of O_i,[51] and several other reports also attribute emissions in yellow and red (>540 nm) to the presence of O_i in the structure because there are different possibilities of oxygen atoms occupying interstitial positions.[52−55] The emission spectra samples prepared under Ar are composed of 1.7% of CB-to-VB transitions, 3.3% related to Zn_i, 20.8% of electrons trapped in V_O decaying to the VB, and 42.2 and 32% of transitions from electrons from the CB decaying to the deep levels of V_{Zn} and O_i, respectively.

Figure 6b shows a film's emission spectra deposited under O_2 without further heat treatment (ZnO-O_2-RT). This spectrum does not show the peak of the transition from the CB to the VB, and in this sample, the transitions related to V_O represent 8.7% while O_i is 91.3% of the spectrum. After heat

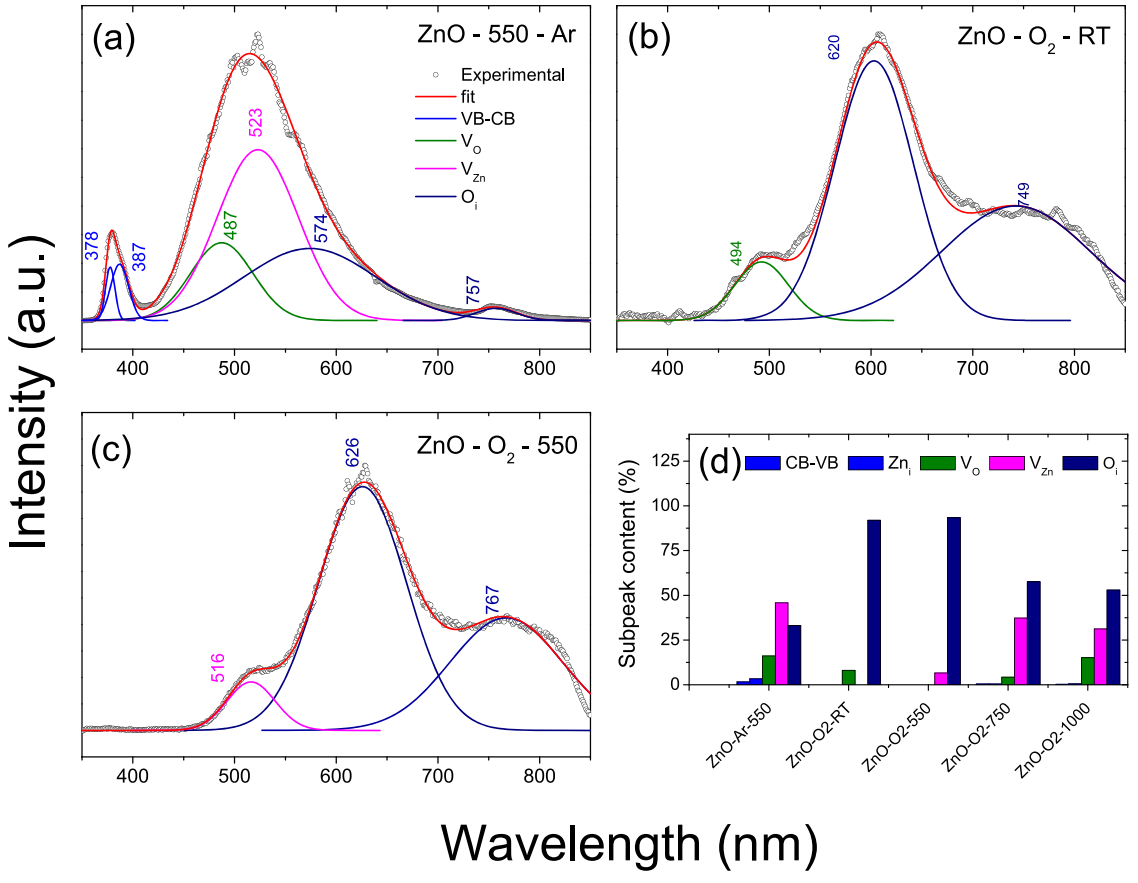

Figure 6. PL spectra of samples prepared under (a) Ar-550 °C, (b) O_2-RT, and (c) O_2-550°C. (d) Subpeak contribution to the emission spectra in %.

https://dx.doi.org/10.1021/acsaelm.1c00058
ACS Appl. Electron. Mater. XXXX, XXX, XXX−XXX

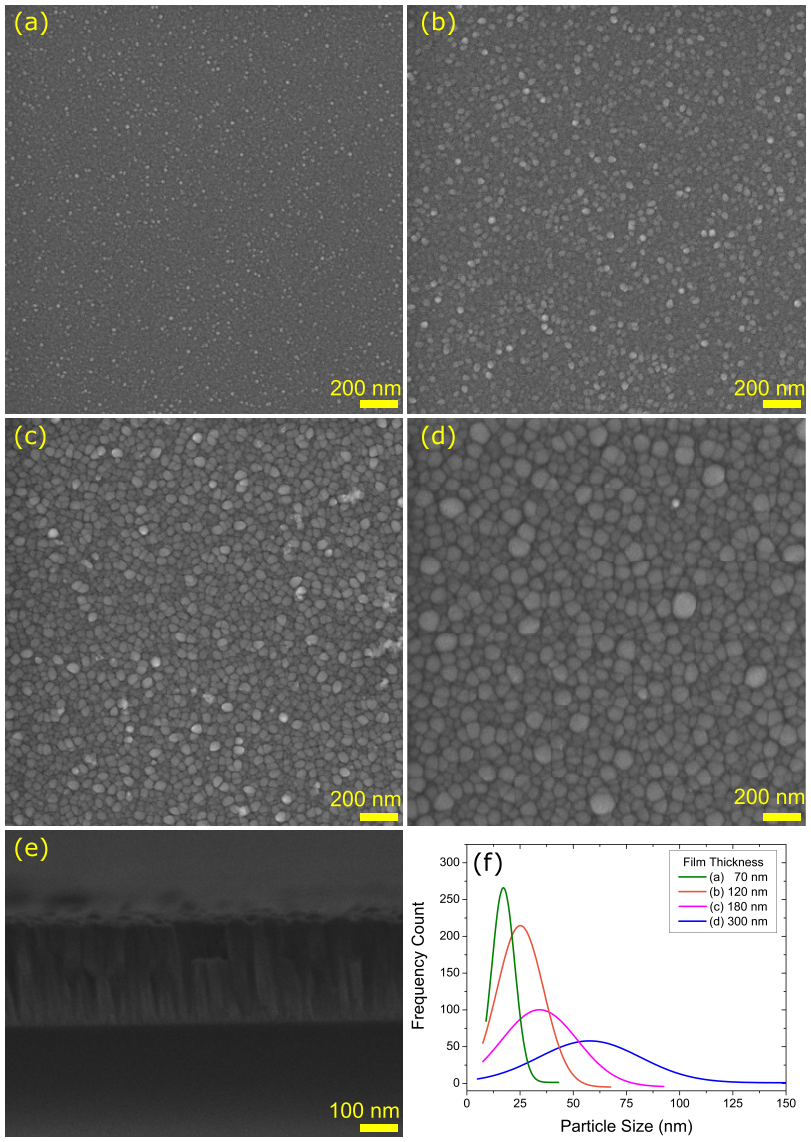

Figure 7. (a–d) SEM images obtained from Zn films deposited under O_2 with different thicknesses heat treated at 550 °C. (e) Cross section exhibiting a columnar growth of the films and (f) particle size distribution of these films with an average size of 18, 28, 38, and 63 for the thickness of 70,120, 180, 300 nm, respectively.

treating in 550 °C, Figure 6c, the amount of emissions related to V_{Zn} represents 6.9%, and O_i is 93.1%. These results suggest that the structure is highly disordered and the heat treatment at 550 °C does not promote any structural reorganization, which is in agreement with the XRD data. After heat treating at 750 and 1000 °C, the emission related to transition between the CB and VB is present and accounts for 0.5 and 0.3%, respectively, and the emissions related to Zn_i for 0.4 and 0.6%, respectively. These samples also show emissions related to V_O (4.2 and 15.1%), V_{Zn} (37.3 and 31.2%), and O_i (57.6 and 52.9%) at 750 and 1000 °C, respectively. The contribution of each emission component is summarized in Figure 6d. Interestingly, the emission band at around 760 nm is not present in samples heat treated at temperatures higher than 550 °C, suggesting that some level of structural reorganization can be achieved at temperatures higher than 550 °C. The evolution of the spectra with temperature can be seen in Figure S5.

3.5. Morphology of ZnO Films Prepared under O_2. Figure 7 presents SEM micrographs of Zn films deposited under an O_2 atmosphere with different thicknesses, namely, (a) 70, (b) 120, (c) 180, and (d) 300 nm. It is important to note that the deposition rates under O_2 are much lower than the deposition rates under Ar. Using the deposition parameters described in Section 2.1, we have found a deposition rate of approximately 100 nm/min for pure Ar and 100 nm/h for pure O_2. Figure 7e shows the cross section of the film with a thickness of 300 nm, and one can note a columnar growth, suggesting that these films should exhibit a certain degree of preferential orientation or texture, which could explain the missing peaks related to the *c* plane observed in the XRD data. In Figure 7a–d, one can note that the average particle size increases with increasing film thickness. Figure 7f shows the particle size distribution after counting 350 particles shown in these micrographs. The average particle sizes are 18, 28, 38, and 63 for thicknesses of 70,120, 180, and 300 nm, respectively.

3.6. Gas Sensing Properties. In order to explore the gas sensing properties of the disordered ZnO films, the sensing devices were fabricated as described in Section 2.4, and their

https://dx.doi.org/10.1021/acsaelm.1c00058
ACS Appl. Electron. Mater. XXXX, XXX, XXX–XXX

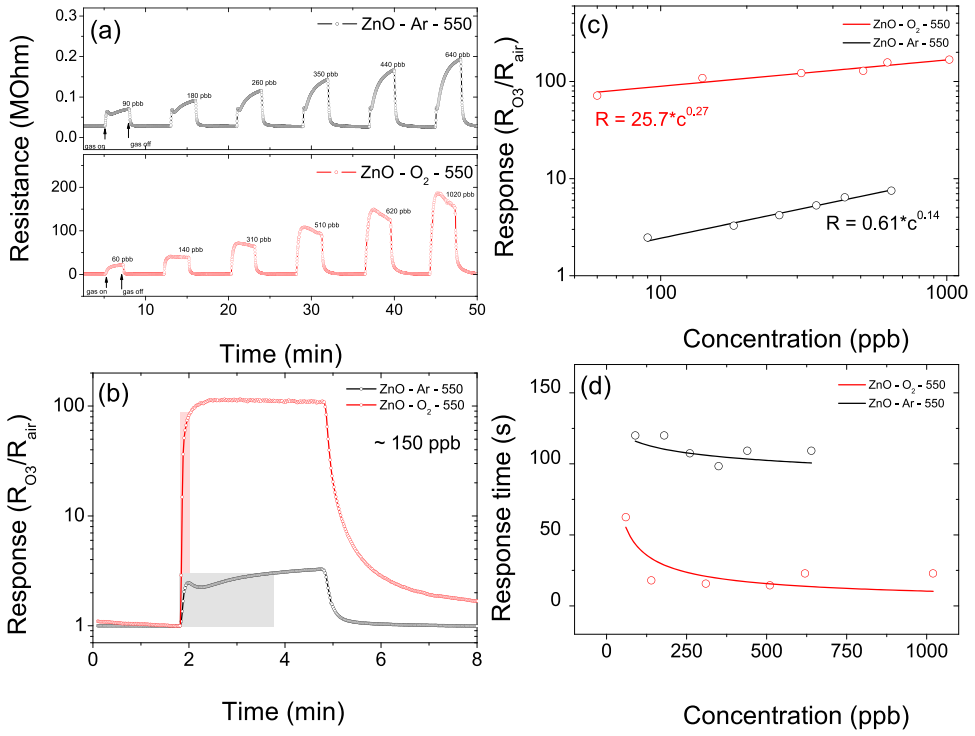

Figure 8. Comparison of the O_3 sensing properties of disordered (red) and conventional (black) ZnO. (a) Dynamic response−recovery curves for controlled exposure of O_3, (b) response−recovery curve for ∼150 ppb exposure, (c) power-law fit, and (d) response time as function of O_3 concentration; lines represent eye guides.

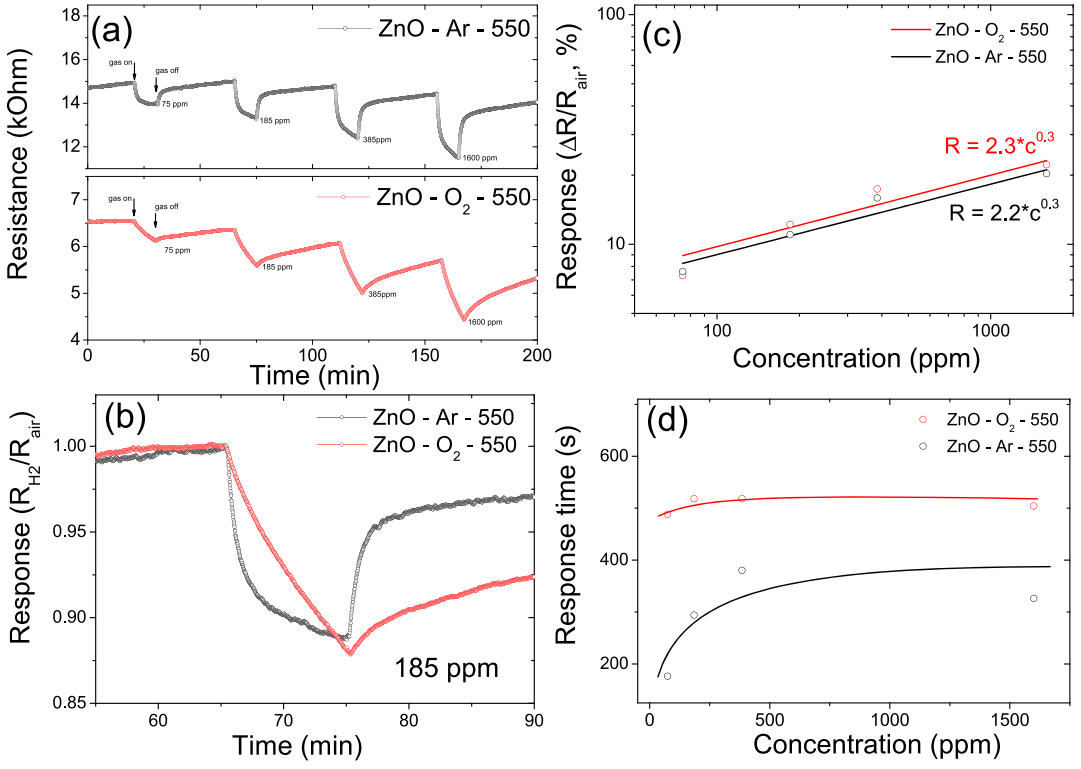

Figure 9. Comparison of the H_2 sensing properties of disordered (red) and conventional (black) ZnO. (a) Dynamic response−recovery curves for controlled exposure of H_2, (b) response curve for 185 ppm exposure, (c) power-law fit, and (d) response time estimative as a function of H_2 concentration; lines represent eye guides.

electrical resistance was monitored under a constant flux of dry air of 100 sccm upon controlled exposure of O_3 and H_2, which were chosen to study the dynamics of O^- ion adsorption/consumption in the devices' surface. Figure 8 presents the dynamic response−recovery upon O_3 exposure. Figure 8a shows the dynamic resistance response−recovery curves

https://dx.doi.org/10.1021/acsaelm.1c00058
ACS Appl. Electron. Mater. XXXX, XXX, XXX−XXX

response of thin films (50 ± 25 nm) deposited under Ar and O_2 toward six cycles of different concentrations of O_3 exposure for 3 min. Figure 8b compares the response (R_{O3}/R_{air}) of both samples toward approximately 150 ppb of O_3. It is possible to observe that the samples prepared under O_2 have a much higher response toward ozone than conventional ZnO. It has been shown that defects play an important role in the gas sensing properties of semiconducting metal oxides because they can be depicted as chemisorption sites for oxygen ions.[53,56] Hence, the improvement in the response toward oxidizing gases should be enhanced due to a richer surface for the chemisorption of these ions. Figure 8c shows the log−log plot of the response versus concentration. Our results are well adjusted by the power law $R = aC^n$, where R is the response, C is the concentration, and a and n are constants. The power coefficient n is 0.14 and 0.27 for the conventional and disordered ZnO, respectively. This power-law fit has been pointed as a consequence of the charge transfer process between the gas and the SMOx surface. Also, n is strongly dependent on the preparation conditions,[36] which agrees with our results since we compare two different preparation conditions that are yielding different n values. The more significant difference between our samples is related to coefficient a, which is 0.6 to conventional ZnO and 25.7 to disordered ZnO. This difference is a consequence of a surface richer in chemisorption sites. In Figure 8d, it is possible to observe that the response time is considerably shorter for disordered ZnO than for conventional ZnO. Also, the response time decreases as the concentration of O_3 increases because a higher O_3 concentration means more adsorption sites can be consumed simultaneously, and more electrons from the ZnO surface are consumed. According to Yamazoe and Shimanoe's theory,[35] the gas sensing mechanism at 300 °C ZnO under O_3 exposure is related to the semiconductor surface adsorption of O^- ions as described below.

$$O_3(gas) + e^-_{surface} \rightarrow O_2(gas) + O^-_{surface} \quad (1)$$

Figure 9 presents the gas sensing properties of these materials upon H_2 controlled exposure. Figure 9a exhibits each sample's dynamics response−recovery curve upon exposure of four different concentrations of H_2. Also, according to Yamazoe and Shimanoe's theory,[35] the gas sensing mechanism at 300 °C ZnO under H_2 exposure is related to the semiconductor surface adsorption of O^- ions as follows.

$$H_2(gas) + O^-_{surface} \rightarrow H_2O(gas) + e^-_{surface} \quad (2)$$

In this case, it is important to mention that the presence of O^- ions at the surface is related to the O_2-rich atmosphere in which the sensor device is, which can be described by the following equation:

$$O_2(gas) + e^-_{surface} \rightarrow 2O^-_{surface} \quad (3)$$

In Figure 9b, it is possible to observe that the disordered ZnO has a much slower response than conventional ZnO, which is also a consequence of a surface with higher concentrations of adsorbed O^- species. Another feature of H_2 sensing behavior is the very similar power-law fit for disordered and conventional ZnO, shown in Figure 9c. The main differences are related to the response time shown in Figure 9d. The competitive phenomena between the O^- accumulation from O_2 present in air and O^- consumption due to the presence of H_2 should be considered to explain the slower response of disordered ZnO. The response curve is explained by the net O^- consumption, which should be smaller in samples that have more adsorption of O^- occurring due to the presence of surface defects. Considering that the disordered ZnO have more sites for O^- accumulation, this contribution would decrease the net O^- consumption rate, leading to greater response times. We have measured the response as the resistance variation after 10 min of exposure as we did not observe any saturation in resistance, even at greater exposure times. Hence, the response time values estimated for disordered ZnO samples are underestimated but still greater than the values of conventional ZnO. The International Union of Pure and Applied Chemistry (IUPAC) defines the limit of detection (LOD) of an analytic device as the concentration that yields a response three times higher than the standard deviation (σ) of measurement without the analyte. Considering the results shown in Figures 8c and 9c, one can estimate the limit of detection for O_3 in approximately 15 and 0.2 ppb for conventional and disordered ZnO, respectively. The estimated LOD for H_2 detection is 2.1 and 2.8 ppm for conventional and disordered ZnO, respectively.

4. CONCLUSIONS

This article presented experimental data regarding the RF magnetron sputtering deposition of ZnO under O_2. Under these conditions, ZnO crystallizes in a highly disordered structure as shown by XRD and Raman spectroscopy data. According to the DFT analysis, the presence of both Zn and O in octahedral interstices is responsible for the symmetry break and distortion of the wurtzite structure, which was confirmed by confronting the main features observed in the Raman theoretical and experimental spectra. Photoluminescence and X-ray photoelectron spectroscopies confirmed a high density of point defects such as O and Zn at interstitial sites. To the best of our knowledge, the disorder effect under these conditions is significantly higher than what has been published previously. This highly disordered structure promotes a significant increase in the emission bands in the visible range compared to conventional ZnO thin films. Regarding ZnO gas sensing properties, it is shown that the ZnO selectivity could be tuned by controlling the density of defects of the crystal structure as the disordered films showed a much stronger response toward ozone detection while its properties regarding hydrogen detection are not altered. Our results open new perspectives to study the dynamics of defect formation as a parameter control of ZnO's physical properties. New deposition parameters such as the RF power, deposition temperature, and working pressure should be carefully investigated to control these defects' concentration and study whether these defects can improve the ZnO performance, targeting different gas sensing applications or other applications in general.

■ ASSOCIATED CONTENT

Supporting Information

The Supporting Information is available free of charge at https://pubs.acs.org/doi/10.1021/acsaelm.1c00058.

Structural models used for the DFT calculations and further details on the effect of heat treatment temperature on the XRD patterns, and XPS and PL spectra of disordered ZnO thin films (PDF)

https://dx.doi.org/10.1021/acsaelm.1c00058
ACS Appl. Electron. Mater. XXXX, XXX, XXX−XXX

AUTHOR INFORMATION

Corresponding Author

Bruno Sanches de Lima − *Sao Carlos Institute of Physics, University of Sao Paulo, São Carlos, SP, Brazil*; Phone: +55 16 3373-9672; Email: delima.bs@gmail.com or delima.bs@usp.br

Authors

Paulina R. Martínez-Alanis − *ENFOCAT-IN²UB, Universitat de Barcelona, 08028 Barcelona, Catalunya, Spain*

Frank Güell − *ENFOCAT-IN²UB, Universitat de Barcelona, 08028 Barcelona, Catalunya, Spain*

Weverton Alison dos Santos Silva − *Sao Carlos Institute of Physics, University of Sao Paulo, São Carlos, SP, Brazil*

Maria I.B. Bernardi − *Sao Carlos Institute of Physics, University of Sao Paulo, São Carlos, SP, Brazil*

Naiara L. Marana − *Modeling and Molecular Simulation Group, São Paulo State University, 01049-010 Bauru, SP, Brazil*

Elson Longo − *Department of Chemistry, Federal University of Sao Carlos (UFSCar), 13565-905 São Carlos, SP, Brazil*; orcid.org/0000-0001-8062-7791

Júlio R. Sambrano − *Modeling and Molecular Simulation Group, São Paulo State University, 01049-010 Bauru, SP, Brazil*

Valmor R. Mastelaro − *Sao Carlos Institute of Physics, University of Sao Paulo, São Carlos, SP, Brazil*; orcid.org/0000-0001-9512-4214

Complete contact information is available at: https://pubs.acs.org/10.1021/acsaelm.1c00058

Notes

The authors declare no competing financial interest.

ACKNOWLEDGMENTS

This work was based upon the financial support by Fundação de Amparo à Pesquisa do Estado de São Paulo−FAPESP (grant nos. 2018/07517-2, 2019/22899-1, 2013/07296-2, 2016/25500-4, 2019/12430-6, and 2019/08928-9). The authors are thankful to Máximo Siu Li and Cleber Renato Mendonça for the experiments and discussions regarding the optical properties of the disordered ZnO thin films. P.R.M.-A. and F.G. are grateful to project MAT2017-87500-P and to the Programa Ajut a la Recerca Transversal de l'IN2UB 2018 for the financial support. This project has received funding from the second Research Collaboration Fund 2019 of the Unión Iberoamericana de Universidades.

REFERENCES

(1) Chen, Y. F.; Bagnall, D. M.; Zhu, Z. Q.; Sekiuchi, T.; Park, K. T.; Hiraga, K.; Yao, T.; Koyama, S.; Shen, M. Y.; Goto, T. Growth of ZnO single crystal thin films on c-plane (0 0 0 1) sapphire by plasma enhanced molecular beam epitaxy. *J. Cryst. Growth* **1997**, *181*, 165−169.

(2) Zhang, S. B.; Wei, S. -H.; Zunger, A. Intrinsic n-type versus p-type doping asymmetry and the defect physics of ZnO. *Phys. Rev. B* **2001**, *63*, No. 075205.

(3) Erhart, P.; Klein, A.; Albe, K. First-principles study of the structure and stability of oxygen defects in zinc oxide. *Phys. Rev. B* **2005**, *72*, No. 085213.

(4) Erhart, P.; Albe, K.; Klein, A. First-principles study of intrinsic point defects in ZnO: Role of band structure, volume relaxation, and finite-size effects. *Phys. Rev. B* **2006**, *73*, 205203.

(5) McCluskey, M. D.; Jokela, S. J. Defects in ZnO. *J. Appl. Phys.* **2009**, *106*, No. 071101.

(6) Wang, Z. L. Nanostructures of zinc oxide. *Mater. Today* **2004**, *7*, 26−33.

(7) Son, D.-Y.; Im, J.-H.; Kim, H.-S.; Park, N.-G. 11% Efficient Perovskite Solar Cell Based on ZnO Nanorods: An Effective Charge Collection System. *J. Phys. Chem. C* **2014**, *118*, 16567−16573.

(8) Zhu, L.; Zeng, W. Room-temperature gas sensing of ZnO-based gas sensor: A review. *Sens. Actuators, A* **2017**, *267*, 242−261.

(9) Lee, K. M.; Lai, C. W.; Ngai, K. S.; Juan, J. C. Recent developments of zinc oxide based photocatalyst in water treatment technology: A review. *Water Res.* **2016**, *88*, 428−448.

(10) Webb, J. B.; Williams, D. F.; Buchanan, M. Transparent and highly conductive films of ZnO prepared by RF reactive magnetron sputtering. *Appl. Phys. Lett.* **1981**, *39*, 640−642.

(11) Carcia, P. F.; McLean, R. S.; Reilly, M. H.; Nunes, G. Transparent ZnO thin-film transistor fabricated by rf magnetron sputtering. *Appl. Phys. Lett.* **2003**, *82*, 1117−1119.

(12) Al-Hardan, N. H.; Abdullah, M. J.; Aziz, A. A.; Ahmad, H.; Rashid, M. The effect of oxygen ratio on the crystallography and optical emission properties of reactive RF sputtered ZnO films. *Phys. B (Amsterdam, Neth.)* **2010**, *405*, 1081−1085.

(13) Ondo-Ndong, R.; Ferblantier, G.; Al Kalfioui, M.; Boyer, A.; Foucaran, A. Properties of RF magnetron sputtered zinc oxide thin films. *J. Cryst. Growth* **2003**, *255*, 130−135.

(14) Gao, W.; Li, Z. W. ZnO thin films produced by magnetron sputtering. *Ceram. Int.* **2004**, *30*, 1155−1159.

(15) Chang, J. F.; Kuo, H. H.; Leu, I. C.; Hon, M. H. The effects of thickness and operation temperature on ZnO : Al thin film CO gas sensor. *Sens. Actuators, B* **2002**, *84*, 258−264.

(16) Katsarakis, N.; Bender, M.; Cimalla, V.; Gagaoudakis, E.; Kiriakidis, G. Ozone sensing properties of DC-sputtered, c-axis oriented ZnO films at room temperature. *Sens. Actuators, B* **2003**, *96*, 76−81.

(17) Suchea, M.; Christoulakis, S.; Moschovis, K.; Katsarakis, N.; Kiriakidis, G. ZnO transparent thin films for gas sensor applications. *Thin Solid Films* **2006**, *515*, 551−554.

(18) Tominaga, K.; Yuasa, T.; Kume, M.; Tada, O. Influence of Energetic oxygen bombardment on conductive ZnO films. *Jpn. J. Appl. Phys.* **1985**, *24*, 944−949.

(19) Ito, N.; Oka, N.; Sato, Y.; Shigesato, Y. Effects of Energetic Ion Bombardment on Structural and Electrical Properties of Al-Doped ZnO Films Deposited by RF-Superimposed DC Magnetron Sputtering. *Jpn. J. Appl. Phys.* **2010**, *49*, No. 071103.

(20) Bikowski, A.; Welzel, T.; Ellmer, K. The correlation between the radial distribution of high-energetic ions and the structural as well as electrical properties of magnetron sputtered ZnO:Al films. *J. Appl. Phys.* **2013**, *114*, 223716.

(21) Vidya, R.; Ravindran, P.; Fjellvag, H.; Svensson, B. G.; Monakhov, E.; Ganchenkova, M.; Nieminen, R. M. Energetics of intrinsic defects and their complexes in ZnO investigated by density functional calculations. *Phys. Rev. B* **2011**, *83*, No. 045206.

(22) Meng, F.; Ge, F.; Chen, Y.; Xu, G.; Huang, F. Local structural changes induced by ion bombardment in magnetron sputtered ZnO: Al films: Raman, XPS, and XAS study. *Surf. Coat. Technol.* **2019**, *365*, 2−9.

(23) Toby, B. H.; Von Dreele, R. B. GSAS-II: the genesis of a modern open-source all purpose crystallography software package. *J. Appl. Crystallogr.* **2013**, *46*, 544−549.

(24) Momma, K.; Izumi, F. VESTA 3 for three-dimensional visualization of crystal, volumetric and morphology data. *J. Appl. Crystallogr.* **2011**, *44*, 1272−1276.

(25) Dovesi, R.; Erba, A.; Orlando, R.; Zicovich-Wilson, C. M.; Civalleri, B.; Maschio, L.; Rerat, M.; Casassa, S.; Baima, J.; Salustro, S.; Kirtman, B. Quantum-mechanical condensed matter simulations with CRYSTAL. *Wiley Interdiscip. Rev.: Comput. Mol. Sci.* **2018**, *8*, No. e1360.

(26) Becke, A. D. Density-Funcional Thermochemistry 3. The role of exact exchange. *J. Chem. Phys.* **1993**, *98*, 5648−5652.

(27) Jaffe, J. E.; Hess, A. C. Hartree-fock study of phase-changes in ZnO at High-pressure. *Phys. Rev. B* **1993**, *48*, 7903−7909.
(28) Bredow, T.; Jug, K.; Evarestov, R. A. Electronic and magnetic structure of $ScMnO_3$. *Phys. Status Solidi B* **2006**, *243*, R10−R12.
(29) Zicovich-Wilson, C. M.; Pascale, F.; Roetti, C.; Saunders, V. R.; Orlando, R.; Dovesi, R. Calculation of the vibration frequencies of alpha-quartz: The effect of Hamiltonian and basis set. *J. Comput. Chem.* **2004**, *25*, 1873−1881.
(30) Pascale, F.; Zicovich-Wilson, C. M.; Gejo, F. L.; Civalleri, B.; Orlando, R.; Dovesi, R. The calculation of the vibrational frequencies of crystalline compounds and its implementation in the CRYSTAL code. *J. Comput. Chem.* **2004**, *25*, 888−897.
(31) Marana, N. L.; Casassa, S.; Longo, E.; Sambrano, J. R. Structural, Electronic, Vibrational, and Topological Analysis of Single-Walled Zinc Oxide Nanotubes. *J. Phys. Chem. C* **2016**, *120*, 6814−6823.
(32) Marana, N. L.; Casassa, S. M.; Sambrano, J. R. Piezoelectric, elastic, Infrared and Raman behavior of ZnO wurtzite under pressure from periodic DFT calculations. *Chem. Phys.* **2017**, *485-486*, 98−107.
(33) Decremps, F.; Datchi, F.; Saitta, A. M.; Polian, A.; Pascarelli, S.; Di Cicco, A.; Itie, J. P.; Baudelet, F. Local structure of condensed zinc oxide. *Phys. Rev. B* **2003**, *68*, 104101.
(34) Ozgur, U.; Alivov, Y. I.; Liu, C.; Teke, A.; Reshchikov, M. A.; Dogan, S.; Avrutin, V.; Cho, S. J.; Morkoc, H. A comprehensive review of ZnO materials and devices. *J. Appl. Phys.* **2005**, *98*, No. 041301.
(35) Yamazoe, N.; Shimanoe, K. Theory of power laws for semiconductor gas sensors. *Sens. Actuators, B* **2008**, *128*, 566−573.
(36) Hua, Z.; Li, Y.; Zeng, Y.; Wu, Y. A theoretical investigation of the power-law response of metal oxide semiconductor gas sensors I: Schottky barrier control. *Sens. Actuators, B* **2018**, *255*, 1911−1919.
(37) Kisi, E. H.; Elcombe, M. M. Upsilon-parameters for the wurtzite structure of ZnS and ZnO using powder neutron-diffraction. *Acta Cryst.* **1989**, *45*, 1867−1870.
(38) Russo, V.; Ghidelli, M.; Gondoni, P.; Casari, C. S.; Bassi, A. L. Multi-wavelength Raman scattering of nanostructured Al-doped zinc oxide. *J. Appl. Phys.* **2014**, *115*, No. 073508.
(39) Cerqueira, M. F.; Viseu, T.; de Campos, J. A.; Rolo, A. G.; de Lacerda-Aroso, T.; Oliveira, F.; Bogdanovic-Radovic, I.; Alves, E.; Vasilevskiy, M. I. Raman study of insulating and conductive ZnO:(Al, Mn) thin films. *Phys. Status Solidi A* **2015**, *212*, 2345−2354.
(40) Guell, F.; Osso, J. O.; Goni, A. R.; Cornet, A.; Morante, J. R. Synthesis and optical spectroscopy of ZnO nanowires. *Superlattices Microstruct.* **2009**, *45*, 271−276.
(41) Huang, G. Y.; Wang, C. Y.; Wang, J. T. First-principles study of diffusion of zinc vacancies and interstitials in ZnO. *Solid State Commun.* **2009**, *149*, 199−204.
(42) Gsiea, A. M.; Goss, J. P.; Briddon, P. R.; Al-habashi, R. M.; Etmimi, K. M.; Marghani, K. A. Native Point Defects in ZnO. *Int. J. Math. Comput. Phys. Elec. Comput. Eng.* **2014**, *8*, 127−132.
(43) Al-Gaashani, R.; Radiman, S.; Daud, A. R.; Tabet, N.; Al-Douri, Y. XPS and optical studies of different morphologies of ZnO nanostructures prepared by microwave methods. *Ceram. Int.* **2013**, *39*, 2283−2292.
(44) Dupin, J. C.; Gonbeau, D.; Vinatier, P.; Levasseur, A. Systematic XPS studies of metal oxides, hydroxides and peroxides. *Phys. Chem. Chem. Phys.* **2000**, *2*, 1319−1324.
(45) Liu, H. Y.; Zeng, F.; Lin, Y. S.; Wang, G. Y.; Pan, F. Correlation of oxygen vacancy variations to band gap changes in epitaxial ZnO thin films. *Appl. Phys. Lett.* **2013**, *102*, 181908.
(46) Guo, H. L.; Zhu, Q.; Wu, X. L.; Jiang, Y. F.; Xie, X.; Xu, A. W. Oxygen deficient ZnO 1-x nanosheets with high visible light photocatalytic activity. *Nanoscale* **2015**, *7*, 7216−7223.
(47) Makula, P.; Pacia, M.; Macyk, W. How To Correctly Determine the Band Gap Energy of Modified Semiconductor Photocatalysts Based on UV-Vis Spectra. *J. Phys. Chem. Lett.* **2018**, *9*, 6814−6817.
(48) Ma, J. H.; Huang, Z. M.; Meng, X. J.; Liu, S. J.; Zhang, X. D.; Sun, J. L.; Xue, J. Q.; Chu, J. H.; Li, J. Optical properties of SrTiO3 thin films deposited by radio-frequency magnetron sputtering at various substrate temperatures. *J. Appl. Phys.* **2006**, *99*, No. 033515.
(49) Spinelli, A.; Torija, M. A.; Liu, C.; Jan, C.; Leighton, C. Electronic transport in doped $SrTiO_3$: Conduction mechanisms and potential applications. *Phys. Rev. B* **2010**, *81*, 155110.
(50) Janotti, A.; Van de Walle, C. G. Native point defects in ZnO. *Phys. Rev. B* **2007**, *76*, 165202.
(51) Wang, M. S.; Zhou, Y. J.; Zhang, Y. P.; Kim, E. J.; Hahn, S. H.; Seong, S. G. Near-infrared photoluminescence from ZnO. *Appl. Phys. Lett.* **2012**, *100*, 101906.
(52) Guell, F.; Martinez-Alanis, P. R. Tailoring the Green, Yellow and Red defect emission bands in ZnO nanowires via the growth parameters. *J. Lumin.* **2019**, *210*, 128−134.
(53) Zhou, X. Y.; Wang, A. Q.; Wang, Y.; Bian, L. Z.; Yang, Z. X.; Bian, Y. Z.; Gong, Y.; Wu, X. F.; Han, N.; Chen, Y. Crystal-Defect-Dependent Gas-Sensing Mechanism of the Single ZnO Nanowire Sensors. *Acs Sensors* **2018**, *3*, 2385−2393.
(54) Han, N.; Hu, P.; Zuo, A.; Zhang, D. W.; Tian, Y. J.; Chen, Y. F. Photoluminescence investigation on the gas sensing property of ZnO nanorods prepared by plasma-enhanced CVD method. *Sens. Actuators, B* **2010**, *145*, 114−119.
(55) Motaung, D. E.; Mhlongo, G. H.; Nkosi, S. S.; Malgas, G. F.; Mwakikunga, B. W.; Coetsee, E.; Swart, H. C.; Abdallah, H. M. I.; Moyo, T.; Ray, S. S. Shape-Selective Dependence of Room Temperature Ferromagnetism Induced by Hierarchical ZnO Nanostructures. *ACS Appl. Mater. Interfaces* **2014**, *6*, 8981−8995.
(56) Al-Hashem, M.; Akbar, S.; Morris, P. Role of Oxygen Vacancies in Nanostructured Metal-Oxide Gas Sensors: A Review. *Sens. Actuators, B* **2019**, *301*, 126845.

NOTE ADDED AFTER ASAP PUBLICATION

This paper was published ASAP on March 11, 2021, with an incorrect version of Figure 6. The corrected version was reposted on March 12, 2021.

https://dx.doi.org/10.1021/acsaelm.1c00058
ACS Appl. Electron. Mater. XXXX, XXX, XXX−XXX